International Journal of Electrical, Electronic and Communication Sciences
ISSN: 2517-9438
Vol:9, No:3, 2015

CFD Analysis of Multi-Phase Reacting Transport Phenomena in Discharge Process of Non-Aqueous Lithium-Air Battery

Jinliang Yuan, Jong-Sung Yu, Bengt Sundén

***Abstract*—**A computational fluid dynamics (CFD) model is developed for rechargeable non-aqueous electrolyte lithium-air batteries with a partial opening for oxygen supply to the cathode. Multi-phase transport phenomena occurred in the battery are considered, including dissolved lithium ions and oxygen gas in the liquid electrolyte, solid-phase electron transfer in the porous functional materials and liquid-phase charge transport in the electrolyte. These transport processes are coupled with the electrochemical reactions at the active surfaces, and effects of discharge reaction-generated solid Li_2O_2 on the transport properties and the electrochemical reaction rate are evaluated and implemented in the model. The predicted results are discussed and analyzed in terms of the spatial and transient distribution of various parameters, such as local oxygen concentration, reaction rate, variable solid Li_2O_2 volume fraction and porosity, as well as the effective diffusion coefficients. It is found that the effect of the solid Li_2O_2 product deposited at the solid active surfaces is significant on the transport phenomena and the overall battery performance.

***Keywords*—**Computational Fluid Dynamics (CFD), Modeling, Multi-phase, Transport Phenomena, Lithium-air battery.

I. Introduction

LITHIUM (Li) battery has attracted much more attention worldwide during the last years as a possible solution for various applications, particularly for electric vehicle (EV) propulsion applications. The present Li-ion battery performance is too low [1]-[3], and increasing research activities have been focused on the ones beyond the Li-ion battery, such as Li-air battery. The Li-air battery comprises of lithium metal anode working as a lithium source supplier, carbon based cathode (with/without catalysts), as well as a separator between them. The fundamental discharge chemistry in Li-air batteries is electrochemical oxidation of lithium metal at the anode and reduction of oxygen from air at the cathode [2]. The generated lithium ions in the anode moves through electrolyte and meet with oxygen obtained from air at the cathode and forms lithium oxide which is accumulated on the porous particles (usually carbon). The Li-air battery cathode microstructure is basically the same as that in PEMFC cathodes, but it usually flooded with liquid electrolytes and should be dehydrated because lithium metal is very sensitive to moisture and aggressively reacts with water [4]. So the Li-air battery is an emerging type of energy storage and conversion device which may be considered as half a battery and half a PEMFC [5].

In non-aqueous Li-air batteries, insoluble lithium peroxide Li_2O_2 (1) and potentially lithium oxide Li_2O (2) are formed in ORR (oxygen reduction reaction) during discharging. With catalysts present, Li_2O_2 might undergo the OER (oxygen evolution reaction) when sufficient high recharge voltages are applied in recharging process. The reactions occur at three-phase boundaries (TPB) involving the solid electrode (for electrons), liquid electrolyte (for Li^+) and dissolved oxygen gas (O_2) in the electrolyte.

$$2Li^+ + 2e^- + O_2 \leftrightarrow (Li_2O_2)_s \qquad E_{rev} = 2.96 \text{ V} \qquad (1)$$

$$4Li^+ + 4e^- + O_2 \leftrightarrow 2(Li_2O)_s \qquad E_{rev} = 2.91 \text{ V} \qquad (2)$$

where E_{rev} is the reversible cell voltage, referenced *vs* Li/Li^+ in this study. The forward reaction in (1) refers to the discharging while the reverse direction stands for the charging process. It is found that Li2O2 is the dominant reaction product in the most recent Li-air battery tests.

Along with experimental studies carried out for different physicochemical properties and the overall performance, theoretical analysis of the electrode structure/morphology and transport phenomena affected by the reaction products is becoming important for achieving high-capacity non-aqueous Li-air batteries. The modeling studies at continuum scale (such as CFD at the battery level) may account for the microscopic material, chemical and morphological properties, which can be a great help to understand the coupled transport phenomena and reactions within the battery for improving its design and optimizing the performance, as well as for identifying their effects on the "sudden death" (i.e., over-potential sharp increase or voltage sharp decrease), and the degradation/failure mechanisms, etc.

The macroscopic or the continuum scale models consider the porous structure as a black box or as a macro-homogeneous porous region (uniformly distributed solid spheres or agglomerates). With suitable boundary conditions specified, a set of governing differential conservation equations for the transport processes can be discretized using conventional CFD techniques, such as finite volume method (FVM), as applied for proton exchange membrane fuel cells [6]. These methods

Jinliang Yuan is with the Department of Energy Sciences, Faculty of Engineering, Lund University, Box 118, 22100 Lund, Sweden (phone: +46 46 222 8413, e-mail: Jinliang.yuan @energy.lth.se).
Jong-Sung Yu works at the Department of Advanced Materials Chemistry, Korea University, 2511 Sejong-ro, Sejong, 339-700, Korea.
Bengt Sundén is with the Department of Energy Sciences, Faculty of Engineering, Lund University, Box 118, 22100 Lund, Sweden.

require much less mathematical efforts and computational resources. However, a big challenge is then put on the issues how to capture the multi–phase transport phenomena by taking into account the effects of solid particle/pore size and complex structural morphology, and the effects of other processes (such as the reactions and solid product formation, etc) in the porous electrodes, see [7] and [8].

One of such models is by Read et al. who conducted a simple analysis to capture the dimensionless oxygen concentration along the cathode length direction. The study is limited only for the steady-state condition with the assumptions that the discharge reaction was first order in the oxygen concentration. The porosity of the electrode did not change with solid Li_2O_2 product generation [9]. While in another study [10], pore volume change due to the discharge product, insoluble Li_2O_2, was modeled by a linear relation and the effect on the oxygen transfer and the cell performance was included, based on the so-called oxygen-limited model. It is because the discharge current density is small, and 1 M concentration of Li^+ in the electrolyte can be simply assumed everywhere in the cathode along the discharge. The conventional Fick's law, together with the continuity equation, was employed for the oxygen transport in the electrolyte, and the ORR kinetic rate was approximated as linearly dependent on the local oxygen concentration. Various models developed for the Li-air batteries are outlined and compared in a recent review work, and it was found that a comprehensive continuum model is significant for understanding the ORR coupled transport phenomena in the Li-air battery electrodes, but only a limited number of the studies are available [11].

It is believed that the transport phenomena and the electrochemical reactions are strongly affected by the microscopic porous structures of the cathodes, as well as the distribution of the ORR generated solid product morphologies and the increased over-potentials. The CFD modeling and analysis methodologies should be developed for understanding the detailed mechanism of the reacting transport phenomena, and for further improvement of battery performance as well as optimizing the design.

In this study, a two-dimensional transient CFD model is developed to capture the reaction coupled transport phenomena characteristics of a Li-air battery using organic electrolytes during the discharge process. The solid Li_2O_2 product structures and physicochemical properties, as well as the effective transport properties, are evaluated and implemented in the model for the Li-air battery. The effect of Li_2O_2 product deposition is considered in terms of a reduction in ORR rate kinetics (active area surface area), porosity distribution and further effective diffusion coefficient, as well as an increase in the charge transfer resistance in the Li_2O_2 product (causing extra voltage reduction).

II. Mathematic Equations

Li^+ and oxygen molecules are dissolved in the electrolyte. The oxygen in the air travels from the gas channel (between the ribs) to the active sites in the cathode, while the Li^+ carry charges between the electrodes. The mathematical description of the transport processes in the Li-air batteries involves the governing equations for the conservation of the electrons, the dissolved ions and oxygen gas coupled with the reaction kinetics in the electrodes. These governing equations will be further linked with the models for the Li_2O_2 formation and deposition at the cathode, as well as effects on the porosity change inside the cathode and the rate equations for ORR and OER via a reduction in the effective surface area, or/and an extra potential drop across the solid product layer [12], [13].

The model developed in this study is for a two-dimensional configuration, and solved for the distributions of oxygen concentration, Li^+ concentration in the electrolyte, solid- and liquid-phase potentials coupled by the ORR rate, as well as volume fraction of solid product. The computation domain is outlined by the dashed line in Fig. 1.

To simplify the analysis and focus on the major processes and phenomena, the following assumptions are applied: the electrolyte fully fills the pores in the cathode electrolyte, both dissolved oxygen gas and Li^+ transfer in electrolyte (liquid) only; the mass transfer of oxygen and lithium ions is by diffusion and migration only (i.e., the convection is neglected); The generated Li_2O_2 product deposits as a smooth film in the electrode, which is based on that the size of Li_2O_2 particles is typically several orders of magnitude smaller than the size of a Li-air battery electrode; Isothermal condition (a room temperature of 297 K) is applied.

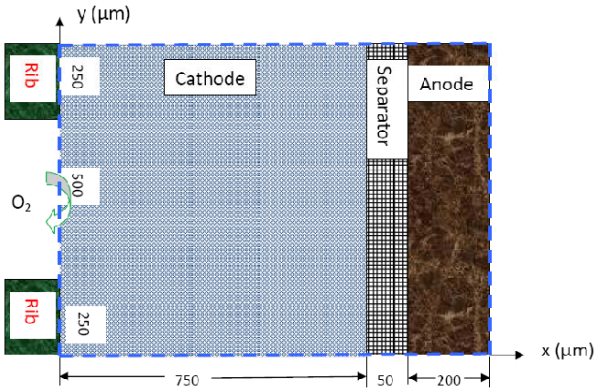

Fig. 1 Configuration and simulation domain of Li-air battery

Li^+ concentration in the electrolyte is usually much higher, e.g., between 1 M and 2M, and often calculated by the concentrated solution approach including the diffusion and migration terms (without convection term) [12]-[15]:

$$\frac{\partial(\varepsilon\rho_{EL}\omega_{Li^+})}{\partial t} = \nabla\cdot(\rho_{EL}D^{eff}_{Li^+}\nabla\omega_{Li^+}) + \frac{\nabla(\rho_{EL}i_l t_+)}{z_+ v_+ F} + \dot{m}_{Li^+} \quad (3)$$

where ω_{Li^+} is the bulk mass fraction of Li^+ in the solution phase which is averaged over the volume of the electrolyte in the pores, ε the porosity of the electrolyte in the cathode and separator. The porosity is constant in separator, but varies in the cathode depending on the deposition of Li_2O_2, t_+ the transference number of Li^+, z_+ and v_+ are the charge number and

reaction stoichiometric coefficient of Li^+, respectively. i_l is the current density in the solution phase or electrolyte current density, $D_{Li^+}^{eff}$ the effective diffusion coefficient, F Faraday's constant (96 485 C/mol). The source (sink) term can be calculated as:

$$\dot{m}_{\mathrm{Li}^+} = \frac{aj_i}{F} M_{\mathrm{Li}} \tag{4}$$

the subscript i is the index to identify the anode or cathode, a the specific surface area of the electrode (specific interfacial area of the pores per unit volume of the total electrode), M the molecular weight, and j the electrode local charge transfer current density at the reaction sites in the electrodes. For discharge operation, $\dot{m}$ will be a source term for the anode and a sink for the cathode. It is so because the ORR happens during the discharge and OER during the charge process in the cathode. However the term should be zero in the separator.

In a typical Li-air battery, the concentration of dissolved oxygen in the electrolyte is very low (a few mM) compared to that of Li^+, mainly due to the low solubility of oxygen. Most of existing cathodes in the literature are fully electrolyte-flooded and only oxygen as the gaseous species is dissolved in the electrolyte. In this case, the Fickian diffusion equation can be employed for oxygen transport.

$$\frac{\partial(\varepsilon\rho_{\mathrm{EL}}\omega_{\mathrm{O}_2})}{\partial t} = \nabla\cdot(\rho_{\mathrm{EL}} D_{\mathrm{O}_2}^{eff}\nabla\omega_{\mathrm{O}_2}) + \dot{m}_{\mathrm{O}_2} \tag{5}$$

The source (sink) term in the oxygen mass conservation equations can be calculated from:

$$\dot{m}_{\mathrm{O}_2} = \frac{aj_c}{F} M_{\mathrm{O}_2} \tag{6}$$

It should be noted that, in a Li-air cathode, oxygen is consumed during discharge (ORR), while the source term should be zero in the separator and anode.

The local charge transfer current density is calculated based on the charge transfer equations. The charge potential in a Li-air cell can be divided into two parts, i.e., the solid-phase potential (φ_s) and the liquid-phase potential (φ_l). It is a fact that the solid-phase potential (by electrons) is only present in the solid material particles in the cathode, the current collectors and the anode, but not in the separator. However the liquid-phase potential is connected to the electrolyte, which exists in the cathode and separator. The solid-phase potential or the potential of electron is governed by the electron movement (or the Ohm's law) in the cathode solid materials and in the anode as [14], [15]:

$$\nabla\cdot(\sigma_e^{eff}\nabla\varphi_s) = \nabla\cdot i_s = S_s \tag{7}$$

where σ_e^{eff} is the effective conductivity of electrons in the cathode carbon material. S_s is the source/sink term for the potential of the electron transfer:

$$S_s = aj_c \text{ in the carbon cathode; = 0 in the other regions} \tag{8}$$

The liquid-phase electric potential refers to the one by the Li^+, which is more complex due to Li^+ movement in concentrated electrolyte. In this study, an equation derived for liquid-phase electric potential from Gibbs-Duhem relation is employed, as in [14], [15]:

$$\nabla\cdot(\sigma_l^{eff}\nabla\varphi_l) - \nabla\cdot\left\{\frac{2\sigma_l^{eff}RT}{F}(1-t_+)[1+\frac{d(\ln f)}{d(\ln c_{\mathrm{Li}^+})}]\frac{1}{c_{\mathrm{Li}^+}}\nabla c_{\mathrm{Li}^+}\right\} = \nabla\cdot i_l = S_l \tag{9}$$

where σ_l^{eff} is effective conductivity of Li^+ in the electrolyte, φ_l the electrolyte potential (or the potential for Li^+ in the electrolyte), and f refers to the activity coefficient of salt in the electrolyte, such as $LiPF_6$. S_l is the source/sink term for the ion potential in the electrolyte:

$$S_l = aj_c \text{ in the cathode electrolyte; = 0 in the other regions} \tag{10}$$

For the electrochemical reaction at the interface between the lithium metal anode and the electrolyte, it is expressed as:

$$j_a = i_0\left[\exp\left(\frac{(1-\beta)nF}{RT}\eta_a\right) - \exp\left(\frac{-\beta nF}{RT}\eta_a\right)\right] \tag{11}$$

here i_0 is the exchange current density for the anode, β refers to the symmetry factor equal to 0.5, η_a the over-potential (or the potential loss) for the reaction at the anode,

$$\eta_a = (\varphi_s - \varphi_l)_a - E_a^{rev} \tag{12}$$

the reaction rate at the TPBs in the cathode is calculated as in [12], [16]:

$$j_c = \frac{2k_{\mathrm{ORR}}\varepsilon_{\mathrm{O}_2}c_{\mathrm{O}_2,s}}{\bar{r}_{\mathrm{p}}c_{\mathrm{O}_2,s}^{ref}}\left\{\exp\left(\frac{2(1-\beta)F}{RT}\eta_c\right) - \exp\left(\frac{2\beta F}{RT}\eta_c\right)\right\} \tag{13}$$

where j_c is the exchange current density for the cathode, $c_{i,s}$ the molar concentration of species i at the solid surface of cathode, k the electrode reaction rate constant, $c_{\mathrm{O}_2}^{ref}$ =1 M is a normalization parameter, while η_c the local over-potential (or the potential loss) at the cathode, which is evaluated by:

$$\eta_c = (\varphi_s - \varphi_l)_c - \Delta\varphi_{film} - E_c^{rev} \tag{14}$$

here $\Delta\varphi_{film}$ is the extra voltage drop across the solid product Li_2O_2 formed during the ORR. In the current study, the following empirical correlation is applied, based on the assumption that the Li_2O_2 product is deposited uniformly on the surfaces of the parallel carbon channels, see [12], [16]:

$$\Delta\varphi_{film} = j_c R_{film} \bar{r}_{p,0} \sqrt{\varepsilon/\varepsilon_0} \ln\sqrt{\varepsilon_0/\varepsilon} \quad (15)$$

where ε_0 and $\bar{r}_{p,0}$ are the initial porosity and average pore radius (at time $t = 0$) obtained for the cathode, respectively. The Li_2O_2 film electronic resistivity, R_{film}, is a fitting parameter exponentially depending on the film thickness [17].

Much like in the fuel cell models, the effective diffusion coefficient D^{eff} and charge transfer conductivity σ^{eff} in the above governing equations are correlated by the so-called Bruggeman method involving the porosity and tortuosity (taking the effective diffusion coefficient as the example):

$$D_i^{eff} = \frac{\varepsilon}{\tau} D_i \quad (16)$$

The evolution of the microscopic porous structure over the operating time is evaluated by a change in various macroscopic parameters in this study, to consider the clogging and passivition effects on the species transport to/from, as well as the reactions at the active sites. The change in the local porosity is evaluated as [10], [12], [18]:

$$\frac{\partial\varepsilon}{\partial t} = -a j_c \frac{M_{Li_2O_2}}{2F\rho_{Li_2O_2}} \quad (17)$$

and the volume fraction of the generated solid product (Li_2O_2) is further determined by:

$$\varepsilon_{Li_2O_2} = 1 - \varepsilon - \varepsilon_0 \quad (18)$$

while the Li_2O_2 deposition on the active surface of the pores decreases the average pore radius in time, which is captured by [10], [12]:

$$\bar{r}_p = \bar{r}_{p,0} \sqrt{\varepsilon/\varepsilon_0} \quad (19)$$

the correction for the effective surface area reduction is then evaluated by:

$$a = a_0 (1 - (\varepsilon_{Li_2O_2}/\varepsilon)^{0.5}) \quad (20)$$

where a_0 is the initial active surface area. It is believed that the discharge process is terminated by a rapid increase of over-potential or a rapid decrease in the voltage at the end of discharge, the so-called "sudden death" of the battery [14].

III. Boundary Conditions and Parameters

As shown in Fig. 1, the computation domain consists of four boundaries and three sub-regions (anode, separator and cathode). Equations (3), (5), (7) and (9) are a set of partial differential equations subject to the boundary and initial conditions.

The top and bottom boundaries (y = 0 and 1000 μm, respectively) are considered to be symmetric and the corresponding boundary conditions are formulated in a general way for all the governing equations:

$$\partial\phi/\partial y = 0 \quad (21)$$

while the boundary conditions for the left- and right-hand boundaries (x = 0 and 1000 μm, respectively) are summarized in Table I.

TABLE I
Boundary Conditions

	x = 0 μm	x = 1000 μm
ω_{Li+}	$\partial\omega_{Li^+}/\partial x = 0$	$\partial\omega_{Li^+}/\partial x = 0$
ω_{O2}	$\omega_{O_2} = \omega_{O_2,s}$ $(250\mu m < y < 750\mu m)$; $\partial\omega_{O_2}/\partial x = 0$	$\partial\omega_{O_2}/\partial x = 0$
φ_s	$-\sigma_e^{eff}\partial\varphi_s/\partial x = I_{load}$	$\partial\varphi_s/\partial x = 0$
φ_l	$\partial\varphi_l/\partial x = 0$	$\partial\varphi_l/\partial x = 0$

No mass flux for Li^+ is specified at both the left- and right hand boundaries (x = 0 and 1000 μm, respectively). While for the dissolved oxygen gas in the electrolyte, its value based on the solubility of oxygen in the electrolyte is specified for the opening part (250 μm < y < 750 μm), and no flux for the remaining parts at the left-hand boundary (x= 0 μm). For the solid-phase potential, the gradient of potential is applied at the left boundary (x = 0 μm), based on the applied current density, see Table I. It should be noted that a continuous condition is specified for the fluxes of all species at the interfaces of the anode/separator (x = 800 μm), and of the cathode/separator (x = 750 μm). The solid-phase electric potential is only computed in the cathode and anode. The voltage of the battery is calculated by the difference between the electrode potential at the left-hand boundary and the electrolyte potential at the interface of the anode and separator, i.e.,

$$V = (\varphi_s)_{x=0} - (\varphi_l)_{x=800\mu m} \quad (22)$$

At the beginning of the discharging process, initial conditions are specified for the Li^+ and oxygen concentrations, the porosity, and the specific interfacial area. These initial values, as well as other parameters applied in this Li-air CFD model, are adopted from literature, as outlined in Table II. Before discharging, the concentration for each species is assumed to be uniformly distributed at all the locations inside the battery and equals to their initial condition values.

IV. Solution Method

In this study, the governing differential equations are converted into algebraic equations using a finite volume method (FVM), see, e.g., [19], and then they are solved by a two-dimensional code, SIMPLE_HT [20]. The code is designed for general convection-diffusion problems, e.g., Navier-Stokes equations and the scalar parameter equations. For pure diffusion problems, such as the transport processes

occurring in Li-air batteries, the transient equations can be solved by this general CFD code.

TABLE II
VALUE OF MAJOR PARAMETERS AND INITIAL CONDITIONS

Parameter	Symbol	Value and Unit
Active area of electrode per volume	a_0	3.67×10^7 m^2 m^{-3}
Exchange current density in cathode	j_c	3.11 A m^{-2}
Transfer coefficient of cathode	β	0.5
Reference concentration of O2 in electrolyte	$\omega_{O2,s}$	9.0×10^{-3} kg kg^{-1}
Initial concentration of lithium ion	$\omega_{Li+,0}$	6.67×10^{-3} kg kg^{-1}
Density of electrolyte	ρ_{EL}	1.0402×10^3 kg m^{-3}
Density of lithium	ρ_{Li}	0.534×10^3 kg m^{-3}
Density of carbon	ρ_C	2.26×10^3 kg m^{-3}
Density of lithium peroxide	ρ_{Li2O2}	2.14×10^3 kg m^{-3}
Density of binder	ρ_{PTFE}	2.2×10^3 kg m^{-3}
Conductivity of electrolyte	σ_l	1.085 Ω^{-1} m^{-1}
Conductivity of electron in the cathode	σ_s	10.0 Ω^{-1} m^{-1}
Conductivity of electron in anode electrode	σ_s	10.0 Ω^{-1} m^{-1}
Diffusivity of oxygen in electrolyte	D_{O2}	3.0×10^{-9} m^2 s^{-1}
Diffusivity of Li^+ in electrolyte	D_{Li+}	2.1×10^{-10} m^2 s^{-1}
Solubility factor of oxygen in electrolyte		0.38
Molecular weight of lithium	M_{Li}	6.94×10^{-3} kg mol^{-1}
Molecular weight of lithium peroxide	M_{Li2O2}	45.88×10^{-3} kg mol^{-1}
Initial Porosity	ε_0	0.73
Electrical resistivity across Li_2O_2 film deposition	R_{film}	1.5×10^8 Ω m^{-1}
Transference number of Li^+	t_+	0.2594
$d(\ln f)/d(\ln c_{Li^+})$		-1.03
Initial particle radius in the electrode	$\bar{r}_{p,0}$	25×10^{-9} m
Length of battery	L	0.001 m
Height of battery	H	0.001 m

The governing equations are first integrated over the control volumes, while the boundary conditions are introduced as the source terms in the control volumes neighboring the boundaries whenever appropriate. The resulting system of algebraic equations is solved using an iterative TDMA (tri-diagonal-matrix-algorithm).

The equations needed for the calculation are coupled by the electrochemical reaction rates, the over-potential, and further the porosity and the specific surface area of the electrode via the source terms and variable physical/transport properties. It should be noted that the generation of Li_2O_2 product is zero in the anode lithium and the separator regions, and non-zero only in the cathode region where the ORR occurs. As mentioned earlier, the physical/transport properties are variable. These parameters depend on the spatial position in the battery, and the discharging states as well. All these parameters are evaluated and updated during iterations of the calculation.

In this investigation, a uniform grid distribution is applied in the y-direction, as well as for the separator and anode regions in the x-direction. To capture the strong reactions and effects on the transport phenomena occurring close to the interface between the cathode and the separator, fine meshes are applied with a non-uniform grid distribution arrangement in the cathode region, as shown in Fig. 2. Here the x* and y* are dimensionless parameters, i.e., $x^* = x/L$ and $y^* = y/H$ (both L and H are the length and the height of the battery).

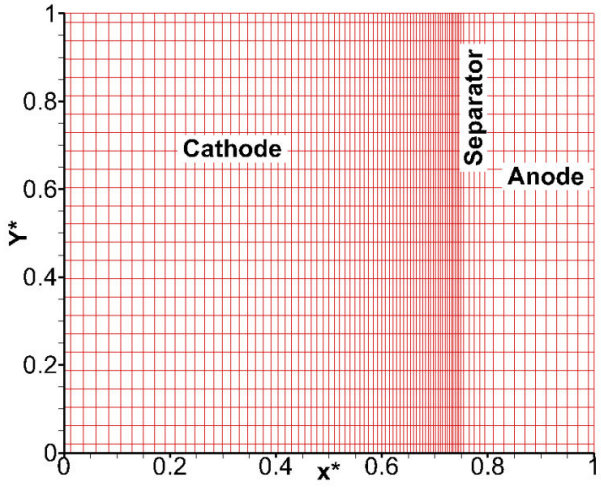

Fig. 2 Mesh arrangement

TABLE III
CASES FOR GRID SENSITIVITY TEST (TIME STEP ΔT = 1 SECOND)

Case	x-direction	y-direction	Expansion factor
Mesh 1	85	24	1/1.03
Mesh 2	**170**	**48**	**1/1.03**
Mesh 3	340	96	1/1.0
Mesh 4	43	12	1/1.04

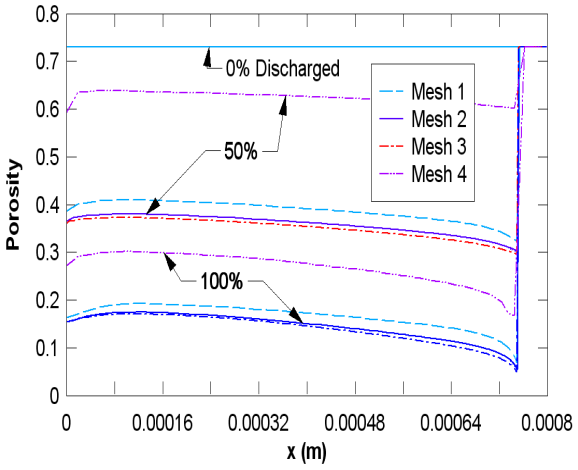

Fig. 3 Performance of mesh arrangement test (time step Δt = 1 second) with different number of meshes and expansion factor

In order to evaluate the performance of the numerical method and the CFD code developed, test calculations considering grid sensitivity (employing different number of control volumes and expansion factors) and time step were carried out, as shown in Table III. The expansion factor smaller than 1 is employed for the cathode region in x-direction, to obtain the fine meshes close to the interface with the separator (see Fig. 2). It is found that the predictions do not change significantly, in terms of the spatial porosity variation (an

important transport parameter in this study as discussed in the following section) along the discharging time, when the number of meshes is increased beyond 170 × 48 (48 for the y-direction, the case Mesh 2 in Table III and Fig. 3). 0% discharged in Fig. 2 refers to a fresh Li-air battery before discharging, while 100% discharged is for the case of fully discharged, or the end of discharge. Consequently, the mesh arrangement of the case Mesh 2 is further applied in this study.

V. Simulation Results and Discussion

After the grid and time-independent tests, the predicted overall battery performance and major parameter distribution of various transport processes are presented and discussed in this section.

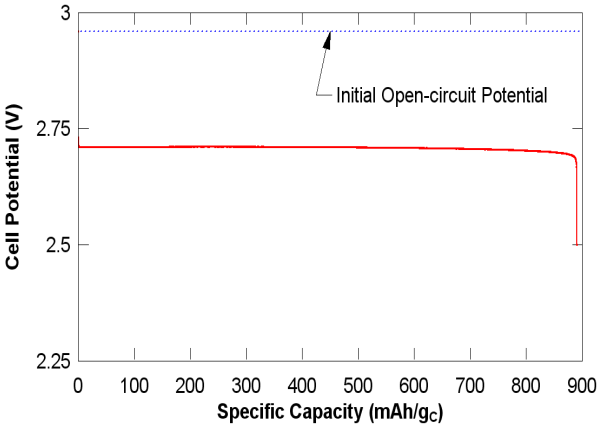

Fig. 4 Li-air battery voltage vs. specific capacity performance achieved at discharge current density of 1 A/m^2

Fig. 4 shows the overall battery performance in terms of voltage change along the specific capacity. The specific capacity is evaluated based on the weight of the carbon material employed in the cathode. As expected, the battery voltage rapidly decreases from its initial value obtained in the reversible condition during the initial discharging. This decrease is due to the result of the activation loss caused by the ORR. It is also found that there is a voltage plateau observed afterwards, followed by a sharp decrease again in voltage at the end of the discharging process, i.e., the so-called "sudden death" of the battery. As discussed later, this is caused by the effect of a reduction in the ORR rate and a reduction in the effective transport properties due to microscopic structure evolution by the Li_2O_2 formation on the active surfaces.

As one of the important features of the current CFD model, the effect of the cathode partial opening at the oxygen inlet side is considered to take the account of the blocking effect on the inlet oxygen distribution by the nickel mesh and the end plates. In contrast, 100% cathode open ratio has been mostly assumed in other simulations in the literature, which is not often employed in either passive or active Li-air battery designs.

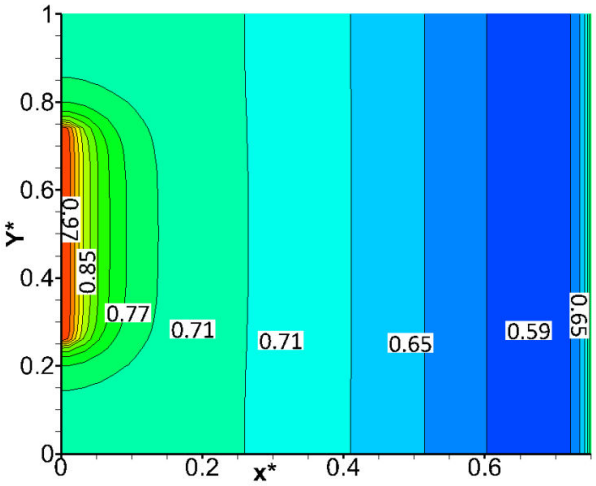

Fig. 5 Predicted oxygen distribution (×10^{-3}) in the cathode after 100% discharged at discharge current density of 1 A/m^2

The spatial oxygen distribution predicted for the battery cathode ($0 < x^* < 0.75$) is presented in Fig. 5. It is found in the figure that dimensionless oxygen mass concentration (the ratio between the local and reference oxygen concentrations) at the cathode inlet region (250 μm < y < 750 μm) at the left boundary (i.e., x=0) is the highest (corresponding to the saturated oxygen dissolved in the electrolyte, i.e., relative oxygen concentration is 1.0), compared with the blocked regions. This is a result of that the oxygen is supplied continuously from the opening at the cathode inlet. It is also found that the oxygen distribution decreases along the battery length direction until somewhere close to the interface between the cathode and the separator, which indicates that the oxygen distribution is not only affected by the mass diffusion in the porous cathode, but also consumed in the ORR during the discharge process. The latter case results in the lowest oxygen concentration in the region where the strongest ORR rates exist, as discussed below.

The porosity distribution in the cathode with a 50% open ratio at the inlet is presented in Fig. 6. As shown in the figure, the porosity at the cathode/air interface (the oxygen inlet, i.e., 250 μm < y < 750 μm and x=0 μm) is lower than that in the remaining parts in the y-direction corresponding to the blocked region (i.e., y < 250 μm and y > 750 μm). This is so because the electrochemical reaction rate in the opening region is higher, consequently the Li_2O_2 generation rates are higher, as discussed later. Further the porosity increases in the x-direction until about 20% of the battery length away from the interface with the separator, and decreases again until the interface between the cathode and the separator. It is also a result of the electrochemical reaction rate varied in the x-direction. It is found that the porosity (and oxygen distribution in Fig. 5) becomes more uniform in the y-direction in the most cathode region away from the inlet side, which indicates that the Li_2O_2 generation rate is also uniform in the major part of the cathode in the x-direction. Consequently the distribution variation of the transport parameters along the x-direction is of most interests.

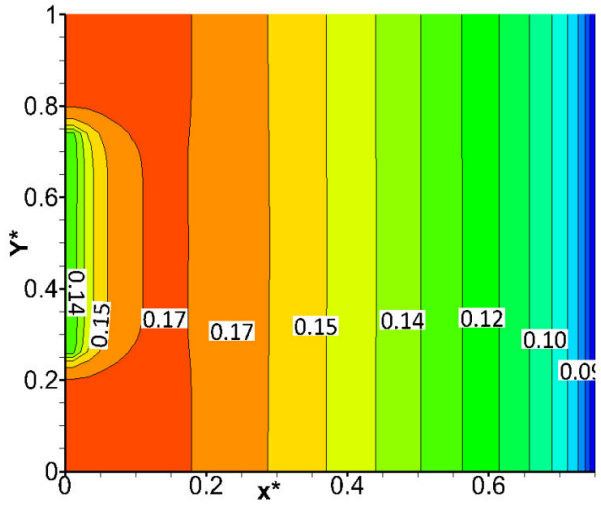

Fig. 6 Predicted spatial porosity distribution in the cathode after 100% discharged at discharge current density of 1 A/m^2

Fig. 7 shows the x-direction local reaction rate averaged along the battery height (the y-direction) for different states of discharging process (such as 1/4, 1/2, 3/4 and 100% discharged). It is found that, when the battery discharges, the ORR rate is slightly higher at the left boundary having the oxygen inlet for all the discharge states, due to the fact that the oxygen is supplied from this side. The ORR rate decreases along with the discharging in the major region of the cathode, which results from the low oxygen concentration consumed by the ORR. On the other hand, the maximum ORR rates are predicted close to the interface between the cathode and the separator, which is believed to conserve the total value of the current going through the battery. The deepest discharging process (100% discharged or the end of discharge) results in the smallest ORR rates, see Fig. 7.

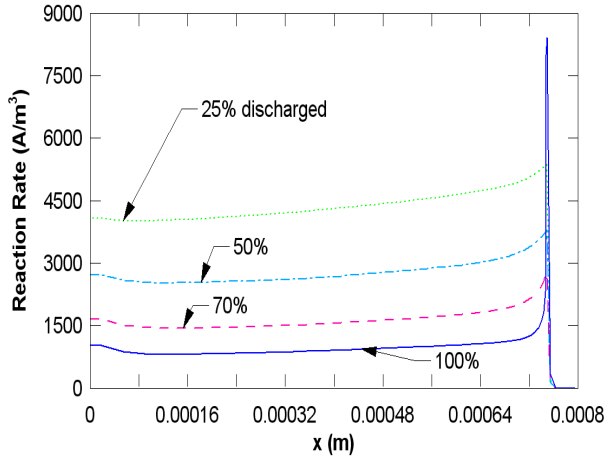

Fig. 7 Predicted local distribution of the ORR rate in the cathode with different discharging state at discharge current density of 1 A/m^2

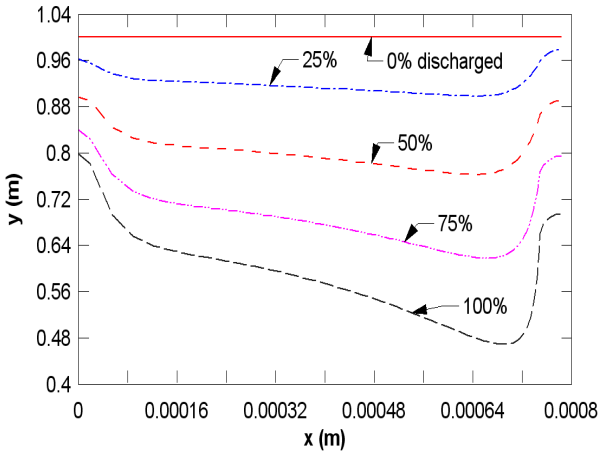

Fig. 8 Predicted spatial distribution of dimensionless oxygen concentration dissolved in the electrolyte with different discharging state at discharge current density of 1 A/m^2

The local oxygen concentration (averaged along the battery height) is presented in Fig. 8 for different discharge states. It is found that a constant relative oxygen concentration ($\omega_{O2}/\omega_{O2,s}$ = 1) is predicted for all the positions along the length direction in the cathode before the battery is discharged (0% discharged in Fig. 8). Along the discharging, the local oxygen concentration decreases with the slight higher values appearing at the left boundary (x = 0, where the oxygen is supplied to the cathode). The lowest oxygen concentrations are predicted close to the interface region between the cathode/separator. This is so partially because the highest reaction rates (then the biggest oxygen consumptions) are found in this region, see Fig. 7. The limiting effects of the oxygen diffusion in the cathode will also contribute to a lower oxygen concentration in the interface region, particularly when the Li_2O_2 product is continuously generated and accumulated on the active surfaces of the porous carbon in the cathode to diminish the available pores for dissolved oxygen transfer in the electrolyte.

The spatial distribution of the porosity in the cathode is shown in Fig. 9. The initial porosity of 0.73 is specified for both the cathode and the separator, as shown by the case of 0% discharged in Fig. 9. As the extent of discharge increases the porosity falls to a very small value between 0.1 to 0.2 when the battery is fully discharged (i.e., 100% discharged in Fig. 9), which limits the diffusion of dissolved oxygen gas in the electrolyte to the battery. Slight lower porosities at the left boundary having the oxygen inlet are again due to the big ORR rates, as presented in Fig. 7, while the smallest porosities predicted for the region close to the interface between the cathode and separator are caused by the maximum ORR rates. It should be noted that the porosity in the separator is not affected by the Li_2O_2 product deposition on the solid surfaces, which is one of the assumptions applied in this study.

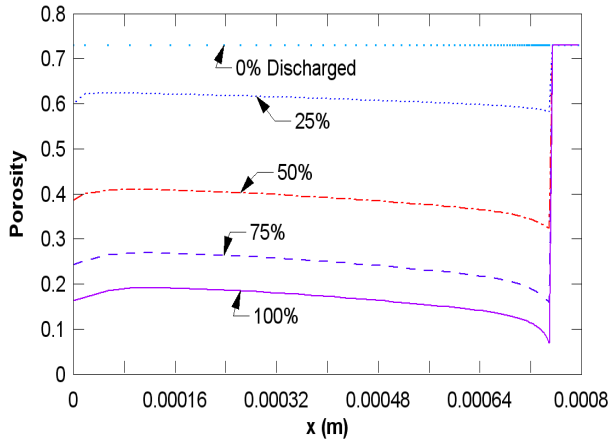

Fig. 9 Local distribution of porosity in the cathode with different discharging state at discharge current density of 1 A/m^2

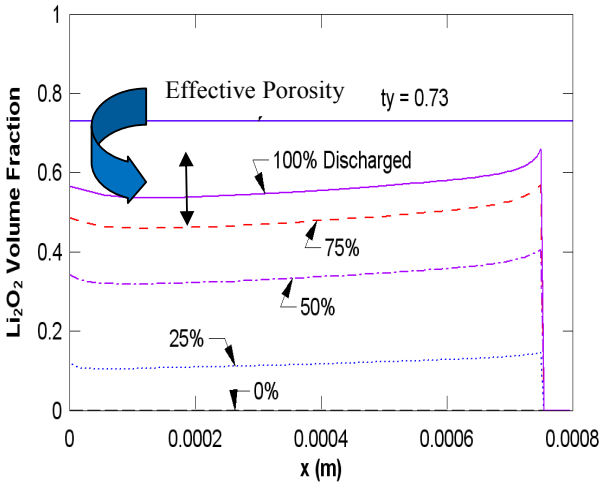

Fig. 10 Spatial distribution of Li2O2 product generation in the cathode with different discharging state at discharge current density of 1 A/m^2

The predicted volume fraction of Li_2O_2 generation is non-uniform, as plotted in Fig. 10, for different discharging states. A slight bigger volume fraction of Li_2O_2 is predicted for all the discharging states at the oxygen inlet, which is believed due to a higher ORR rate. After a slight decrease in the cathode region close to the inlet, the volume fraction of Li_2O_2 increases in the major part of the cathode, until it reaches a maximum value in the region close to the interface with the separator. This maximum volume fraction is about 0.65 obtained for the 100% discharged case, which is higher than those obtained from other discharge states. It is also clear that the variation in the Li_2O_2 volume fraction between 25% and 50% discharge states is the biggest, while that between 75% and 100% discharge states the smallest. The Li_2O_2 solid products deposited at the active surfaces will reduce the void space for the species transport and limit oxygen diffusion in the cathode, as well as bring in an extra potential loss to the activation, which result in a smaller ORR rates.

As also shown in Fig. 10, the effective porosity, defined as the difference between the initial constant porosity and the local Li_2O_2 volume fraction decreases along the discharging process, and the smallest values are obtained when the battery is fully discharged. It is believed that the effective porosity at the oxygen inlet side (x = 0) is much more important, because all of the consumed oxygen during discharging is supplied from this boundary. As a result of the bigger ORR rate in the region close to the separator, Li_2O_2 is produced faster and the effective porosity decreases much more quickly, which gives a bigger resistance for the oxygen diffusion and charge transfer, responsible for the "sudden death" of the battery discharging process.

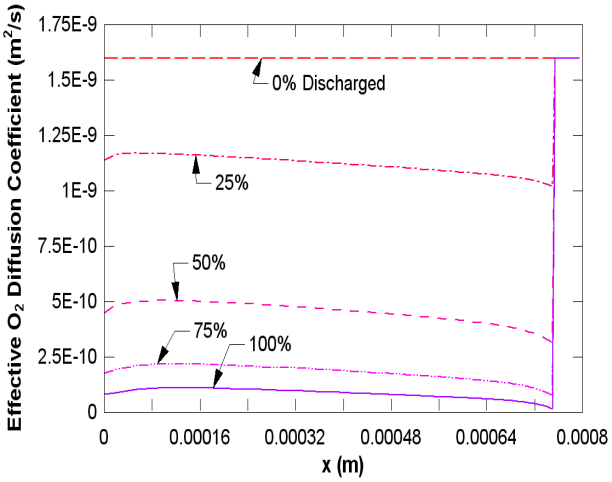

Fig. 11 Spatial distribution of effective oxygen diffusion coefficient in the cathode with different discharging state at discharge current density of 1 A/m^2

Furthermore, the effects of the generated Li_2O_2 product deposition and the microscopic structure evolution on the transport phenomena are correlated to the effective diffusion coefficients. As an example, the spatial distribution of the effective oxygen diffusion coefficient is shown in Fig. 11. It is found that the effective oxygen diffusion coefficient is non-uniform for all of the discharge cases. This coefficient decreases along with the discharging process, as expected. Corresponding to the bigger Li_2O_2 volume fraction, a smaller effective oxygen diffusion coefficient is predicted close to the separator interface. This coefficient is near zero when the battery is fully discharged (100% discharged in Fig. 11). It is believed that the sharp decrease in the overall battery performance (i.e., the voltage vs. the specific capacity in Fig. 4) is mainly caused by a reduction in the effective diffusion coefficient in the cathode, particularly in the region close to the separator.

VI. Conclusions

A two-dimensional transient CFD model is developed and applied to investigate the transport phenomena coupled with the discharge reaction (ORR) at the active carbon surfaces in

the Li-air batteries. Particularly the volume fraction of the ORR-generated solid Li_2O_2 is predicted, and its effects is implemented on the evolution of the microscopic structure and the ORR rate, a reduction in the porosity and the effective species diffusion coefficients in the electrolyte, as well as an increase in the electron conduction resistance and over-potential. It is found that the spatially non-uniform Li_2O_2 volume fractions increase along with the discharging state, and the highest values are obtained at the end of discharge, which is responsible for the sudden death of the battery performance. It is also clear that the effective diffusion coefficients decrease rapidly, particularly in the cathode region close to the separator, due to the fact that the ORR rates in this region is the highest. It is suggested that the transport processes and overall performance of the Li-air battery may be improved if the microscopic structures, such as the porosity distribution, are optimized and applied to better utilize the pores deep in the cathode more efficiently.

ACKNOWLEDGMENT

The financial support from the Swedish Research Council (VR) and the Swedish Foundation for International Cooperation in Research and Higher Education (STINT) is gratefully acknowledged.

REFERENCES

[1] J. Lu, L. Li, J. B. Park, Y. K. Sun, F. Wu and K. Amine, Aprotic and Aqueous Li−O_2 Batteries, *Chem. Rev.*, 114 (2014), pp. 5611−5640.
[2] G. Girishkumar, B. McCloskey, A. C. Luntz, S. Swanson and W. Wilcke, Lithium-Air Battery: Promise and Challenges, *J. Phys. Chem. Lett.*, 1 (2010), pp. 2193–2203.
[3] J. Lu and K. Amine, Recent Research Progress on Non-aqueous Lithium-Air Batteries from Argonne National Laboratory, *Energies*, 6 (2013), pp. 6016-6044.
[4] A. Zahoor, M. Christy, Y. J. Hwang and K. S. Nahm, Lithium Air Battery: Alternate Energy Resource for the Future, *J. Electrochem. Sci. Tech.,* 3 (2012), pp. 14-23.
[5] M. Park, K. Y. Kim, H. Seo, Y. E. Cheon, J. H. Koh, H. Sun and T. J. Kim, Practical Challenges Associated with Catalyst Development for the Commercialization of Li-air Batteries, *J. Electrochem. Sci. and Tech.,* 5 (2014), pp. 1-18.
[6] J. Yuan, M. Rokni and B. Sundén, Buoyancy Effects on Developing Laminar Gas Flow and Heat Transfer in a Rectangular Fuel Cell Duct, *Num. Heat Transfer*: *Part A: Applications*, 39 (2001), pp. 801-822.
[7] J. Yuan and B. Sunden, On Continuum Models for Heat Transfer in Micro/Nano-scale Porous Structures Relevant to Fuel Cells, *Int. J. Heat Mass Transfer*, 58 (2013), pp. 441-456.
[8] J. Yuan and B. Sundén, On Mechanisms and Models of Multi-component Gas Diffusion in Porous Structures of Fuel Cell Electrodes, *Int. J. Heat Mass Transfer*, 69 (2014), pp.358-374.
[9] J. Read, K. Mutolo, M. Ervin, W. Behl, J. Wolfenstine, A. Driedger and D. Foster, Oxygen Transport Properties of Organic Electrolytes and Performance of Lithium/Oxygen Battery, *J. Electrochem. Soc.*, 150 (2003), pp**.** A1351-A1356.
[10] S. S. Sandhu, J. P. Fellner and G. W. Brutchen, Diffusion-limited Model for a Lithium/Air Battery with an Organic Electrolyte. *J. Power Sources*, 164 (2007), pp. 365-371.
[11] J. Yuan, J.-S. Yu and B. Sundén, Review on Mechanisms and Continuum Models of Multi-phase Transport Phenomena in Porous Structures of Non-aqueous Li-Air Batteries, to be submitted.
[12] X. Li and A. Faghri, Optimization of the Cathode Structure of Lithium-Air Batteries Based on a Two-dimensional, Transient, Non-isothermal Model, *J. Electrochem. Soc.*, 159 (2012), pp. A1747-A1754.
[13] P. Tan, Z. Wei, W. Shyy and T. S. Zhao, Prediction of the Theoretical Capacity of Non-aqueous Lithium-air Batteries, *Applied Energy*, 109 (2013), pp. 275-282.
[14] U. Sahapatsombut, H. Cheng and K. Scott, Modelling the Micro-macro Homogeneous Cycling Behaviour of a Lithium-air Battery, *J. Power Sources*, 227 (2013), pp. 243-253.
[15] K. Yoo, S. Banerjee and P. Dutta, Modeling of Volume Change Phenomena in a Li-air Battery, *J. Power Sources*, 258 (2014), pp. 340-350.
[16] P. Andrei, J. P. Zheng, M. Hendrickson and E. J. Plichta, Modeling of Li-Air Batteries with Dual Electrolyte, *J. Electrochem. Soc.*, 159 (2012), pp. A770-A780.
[17] P. Albertus, G. Girishkumar, B. McCloskey, R. S. Sánchez-Carrera, B Kozinsky, J. Christensen and A. C. Luntz, Identifying Capacity Limitations in the Li/Oxygen Battery Using Experiments and Modeling, *J. Electrochem. Soc.*, 158 (2011), pp. A343-A351.
[18] M. Mehta, V. V. Bevara, P. Andrei and J. Zheng, Limitations and Potential Li-Air Batteries: a Simulation Prediction, *The International Conference on Simulation of Semiconductor Processes and Devices* (SISPAD), Sept. 5-7, 2012, Denver, CO, USA.
[19] H. K. Versteeg and W. Malalasekera, An Introduction to Computational Fluid Dynamics, the Finite Volume Method, 2nd edition, Pearson Education Limited, Essex, England, 2007.
[20] B. Sundén, M. Rokni, M. Faghri and D. Eriksson, The Computer Code SIMPLE_HT for the course Computational Heat Transfer, Lund University, 2004.